Proceedings of ASME Turbo Expo 2023
Turbomachinery Technical Conference and Exposition
GT2023
June 26-30, 2023, Boston, Massachusetts, USA

GT2023-101925

COHERENT TURBULENT STRESSES IN UNSTEADY FORCED TRANSONIC NOZZLE WITH SHOCK-INDUCED SEPARATION

Nicolas Goffart[1,*], Benoît Tartinville[1], Sergio Pirozzoli[2]

[1]Cadence Design Systems Belgium, Brussels, Belgium
[2]La Sapienza University of Rome, Rome, Italy

ABSTRACT

The influence of rotor/stator interference on shock-wave/boundary layer interaction is investigated by means of an implicit large-eddy simulation. To replicate actual turbomachinery conditions but at a lower cost, this work considers a transonic bump over which a shock-wave develops and interacts with the separated boundary layer. Moreover, the backpressure is set to fluctuate at a realistic reduced frequency. The analysis is focused on the coherent component of the flow and more particularly the turbulent stresses in the recirculation region. Phase-averaging is performed in order to highlight this component and the reference oscillator is based on the location of the separation point. Statistical convergence is assessed. Coherent turbulent stresses show a two-layers pattern, the upper layer being linked to the mixing layer and the inner layer developing below. The coherent component can reach up to 60% of the local mean value. Budgets show that only some production terms are significant and each of them is acting upon a specific layer of the associated coherent turbulent stress. Finally, pressure strain, responsible for the coupling between the transport equations, is also of importance.

Keywords: bump, transonic, forced, turbulence

NOMENCLATURE

δ_0	Reference boundary layer thickness
$\Delta x, \Delta y, \Delta z$	Grid resolution
U_∞	Reference streamwise velocity

Abbreviations

DNS	Direct Numerical Simulation
FFT	Fast Fourier Transform
(I)LES	(Implicit) Large-Eddy Simulation
SWBLI	Shock-Wave/Boundary Layer Interaction
(U)RANS	(Unsteady) Reynolds-Averaged Navier-Stokes
WALE	Wall-Adapting Local Eddy-Viscosity
WPSD	Weighted Power Spectral Density

Superscripts

$+$	Wall unit
$\overline{}$	Mean component
$\widetilde{}$	Coherent component
$'$	Incoherent component

1. INTRODUCTION

Over the last decades, three-dimensional RANS simulations have been often used in turbomachinery design. However, even if the state-of-the-art RANS can produce accurate results close to design points, it has difficulties at off-design. This is the case near the surge line because of the general drawback of turbulence models to reliably predict secondary flows. This is also the case close to choke conditions because of the complex shock-wave/boundary layer interaction that can appear. Furthermore, modern designs tend towards more compact engines for which the rotor/stator interactions are of great importance. The combination of the resulting strong unsteady pressure signal with the SWBLI is a new challenge for turbomachinery design if better efficiency is desired.

Whereas they are still not accessible in current industrial design chains, high-fidelity computational methods such as LES and DNS are of great interest. They are indeed able to capture complex flow features that (U)RANS simulations cannot [1]. In order to better understand the flow behavior in unsteady forced shock-induced separation occurring in turbomachinery, it is here proposed to use an ILES approach, or under-resolved DNS. To reduce its cost, a transonic bump will be studied instead of a full span 3D blade.

A bump carefully designed to produce the same flow features as in a transonic blade passage [2] has been selected. Experimental as well as numerical results are already available on this configuration. The operating points investigated give rise to a shock-wave that interacts with the detached boundary layer. Furthermore, the influence of an oscillating back-pressure, which mimics the rotor/stator interaction, has also been assessed at various frequencies. The one chosen here - 500 Hz - corresponds to

*Corresponding author: ngoffart@cadence.com

a reduced frequency of 0.4. Both convective and periodic fluctuations are therefore two equally dominant mechanisms as can be found in a turbomachinery context (see [3] for instance).

This bump has already been investigated using either (U)RANS [2] or high-fidelity methods [4–7]. Regarding the latter, only an unperturbed configuration has been studied in [4] using LES method with WALE subgrid scale model. A sensitivity study to the flow condition and the numerical settings (domain height, type of boundary condition) has been performed by the same authors [5]. However, the Reynolds number has been decreased by an order of magnitude compared to the experiment to make the simulations affordable. A DNS of the same bump can be found [6] but at a higher Mach number and again at a lower Reynolds number. The only study that investigates the impact of the oscillating backpressure is presented in [7] using an ILES approach. However, the reduced frequencies considered were one to two orders of magnitude lower than expected. The flow is thus the sum of quasi-steady states and convection is the dominant mechanism.

In light of this, the present paper introduces the results of an ILES of the transonic flow over this bump, with backpressure fluctuating at a realistic reduced frequency. The high-order solver and the computational setup are presented in the first section, together with the data treatment. The results are examined in the second section. The influence of the oscillating backpressure is assessed with a particular emphasis on the harmonic component of turbulent stresses and their budgets.

2. COMPUTATIONAL METHODOLOGY

2.1 Numerical schemes

The high-fidelity simulation is performed using an in-house high-order solver. The spatial discretization is based on the flux reconstruction method introduced in [8]. The approach allows to recover various popular high-order schemes, such as the Discontinuous Galerkin method. The spatial order of accuracy can be directly chosen and a fourth-order of accuracy has been selected. An explicit 5-stages fourth-order accurate Runge-Kutta scheme is used for the temporal derivative following [9].

To be able to accurately capture the shock-wave/boundary layer interaction, special attention should be paid to the shock-capturing technique. The combination of a Laplacian artificial viscosity method [10] with the Ducros sensor [11] makes the approach relatively efficient. Indeed, the addition of the Ducros sensor allows to discriminate the shock region from the boundary layer. It therefore avoids any over-dissipation within the boundary layer and ensures its proper development. Besides shock-capturing, the global robustness has been further enhanced by using a positivity-preserving limiter [12].

Turbulent inflow conditions are prescribed following the digital filtering approach [13] but with a 2D filter correlated in time [14, 15]. Furthermore, the inlet perturbations are scaled following [16].

No explicit sub-grid scale model is used to account for the scales that are not resolved. This approach is referred to as Implicit LES or under-resolved DNS.

The solver has been previously presented and validated on a canonical oblique shock-wave/boundary layer interaction [17]. More details on the numerical method can be found in this paper.

2.2 Flow conditions and simulation setup

The configuration that is investigated is the transonic bump described in [2]. Its length and thickness are 184 mm and 10.48 mm, respectively. The wind tunnel height is 120 mm.

The computational domain is a simple box extending $30\delta_0$ upstream of the bump and $20\delta_0$ downstream. Its width is around $4\delta_0$. Following the experimental measurements in [18], the reference boundary layer thickness δ_0 here is 8.95mm, measured at $x = -0.1$m. This value has also been considered in other numerical studies [4].

The mesh consists of hexahedra. Using the high-order flux reconstruction approach, the grid resolution is evaluated with respect to the solution points, here at polynomial order 3. In the streamwise direction, the cell size is almost constant and leads to $\Delta x^+ = 16$ in viscous units, based on upstream conditions. In order to avoid spurious reflection of high-frequency waves, the mesh is progressively coarsened over the last $10\delta_0$ to reach $\Delta x^+ = 160$. The mesh is uniform in the spanwise direction with $\Delta z^+ = 12$. In the wall normal direction, the mesh is progressively stretched. Bottom and top boundary layers contain 100 solution points each. The first one is located well below $y^+ = 1$. From the edge of the boundary layer and in the freestream the mesh refinement is such that $\Delta y^+ = 16$. Therefore, the total number of degrees of freedom rises to about 80 million.

Because of the limited computing resources, the Reynolds number - based on the bump length - has been reduced to 2×10^5. This is 20 times less than the experimental one. The fluid is air assumed as perfect gas but with a viscosity multiplied by the same factor.

Freestream total quantities are imposed at the inlet. The total pressure is 160 kPa and the total temperature is 300 K. The inlet Mach number is 0.7. Based on these freestream inlet quantities, the reference streamwise velocity U_∞ used hereafter for normalization is ≈ 233m/s. The inlet boundary layer as well as Reynolds stress profiles needed for the rescaling in the generation of turbulent inflow come from a precursor ILES simulation. Various levels of backpressure were investigated in the experiment. The present work is focused on the configuration with a mean outlet static pressure of 106 kPa fluctuating in time following a sine function which amplitude corresponds to 2% of the mean and the frequency of which is 500 Hz. This time-varying value is imposed uniformly along the outlet surface. The top and bottom no-slip walls are assumed adiabatic. Periodic boundary conditions are used in the spanwise direction.

Finally, the explicit time step is set to 4×10^{-8} s. The parameters of the shock-capturing technique (see [17]) are s_0 = -4.5, $\kappa = 1.5$, $C_T = 0.01$ and $s_{D,0} = 0.2$. Density is used as the sensor variable.

2.3 Data acquisition and treatment

After a transient phase, the data for this study, consisting of span-averaged slices, are collected for 10 periods at an output rate of 500 kHz.

The effect of the fluctuating backpressure on the flow field is assessed by extracting its coherent component from the data.

Following the triple decomposition [19], every instantaneous flow quantity q can be written as the sum of three components,

$$q = \overline{q} + \widetilde{q} + q' \tag{1}$$

where $\overline{q}$ is the mean component, $\widetilde{q}$ is the periodic (or coherent) component and q' is the turbulent (or incoherent) component. For this decomposition to be meaningful, the time scales corresponding to the coherent and the incoherent components (which both depend on time, contrary to the mean component) must differ by several orders of magnitude. It is valid in this case since one period at the forcing frequency is 2×10^{-3}s whereas the characteristic time scale of the energetic eddies in the incoming turbulent boundary layer is $O(\delta_0/U_\infty) \approx 3.8 \times 10^{-5}$s.

In this work, the main focus is on the turbulent stresses, which can also follow the triple decomposition

$$u_i'u_j' = \overline{u_i'u_j'} + \widetilde{u_i'u_j'} + \left(u_i'u_j'\right)' \tag{2}$$

Consequently, the influence of the forcing on the turbulence will be seen through $\widetilde{u_i'u_j'}$.

The transport equation for this component of turbulent stresses can be derived [19] and can be re-organized to highlight the contributions of production $\widetilde{P}_{ij}$, pressure strain $\widetilde{T}_{ij}$, dissipation $\widetilde{D}_{ij}$ and diffusion flux $\widetilde{J}_{ij,k}$ [20], which gives

$$\frac{\partial \widetilde{u_i'u_j'}}{\partial t} + \overline{u_k}\frac{\partial \widetilde{u_i'u_j'}}{\partial x_k} + \widetilde{u_k}\frac{\partial \widetilde{u_i'u_j'}}{\partial x_k} = \widetilde{P}_{ij} + \widetilde{T}_{ij} - \widetilde{D}_{ij} - \widetilde{J}_{ij,k} \tag{3}$$

with

$$\widetilde{P}_{ij} = -\left(\widetilde{u_i'u_k'}\frac{\partial \widetilde{u_j}}{\partial x_k} - \widetilde{u_i'u_k'}\frac{\partial \widetilde{u_j}}{\partial x_k} + \overline{u_i'u_k'}\frac{\partial \widetilde{u_j}}{\partial x_k} + \widetilde{u_i'u_k'}\frac{\partial \overline{u_j}}{\partial x_k}\right) - \left(\widetilde{u_j'u_k'}\frac{\partial \widetilde{u_i}}{\partial x_k} - \widetilde{u_j'u_k'}\frac{\partial \widetilde{u_i}}{\partial x_k} + \overline{u_j'u_k'}\frac{\partial \widetilde{u_i}}{\partial x_k} + \widetilde{u_j'u_k'}\frac{\partial \overline{u_i}}{\partial x_k}\right) \tag{4a}$$

$$\widetilde{T}_{ij} = \frac{1}{\rho}\left(\widetilde{p'\frac{\partial u_i'}{\partial x_j}} + \widetilde{p'\frac{\partial u_j'}{\partial x_i}}\right) \tag{4b}$$

$$\widetilde{D}_{ij} = 2\nu\widetilde{\frac{\partial u_i'}{\partial x_k}\frac{\partial u_j'}{\partial x_k}} \tag{4c}$$

$$\widetilde{J}_{ij,k} = \frac{\partial}{\partial x_k}\left(\widetilde{u_i'u_j'u_k'} + \frac{1}{\rho}\widetilde{u_j'p'}\delta_{ik} + \frac{1}{\rho}\widetilde{u_i'p'}\delta_{jk} - \nu\frac{\partial \widetilde{u_i'u_j'}}{\partial x_k}\right) \tag{4d}$$

The flow is assumed to be incompressible when deriving these equations for the coherent motion and ρ is therefore taken as the mean value. The incompressible assumption can seem dubious as a shock-wave develops and therefore the flow is compressible in the freestream. However, the region of interest, that is to say the recirculation, is at low Mach number and as a consequence the compressibility effects are expected to be negligible. This has been a posteriori checked by computing the different terms in the incompressible mean equations of conservation of mass and momentum. It showed that the balance is indeed reached in the downstream part of the bump. The incompressible assumption is therefore reasonable in that region of the flow.

Two averaging operators are needed when using the triple decomposition. Time-averaging is performed to obtain the mean component of the flow and phase-averaging is employed to extract the mean and the coherent components together. The difference between the two therefore allows to isolate the coherent component. In this work, each period is decomposed into ten bins of equal width. The corresponding labeling of the bins, with respect to a reference oscillator, is illustrated in figure 1. The choice of the reference oscillator is discussed in the results section. Finally, it is noted that the use of spatially-averaged data in the homogeneous direction of the flow is of prime interest to improve the convergence of the phase-averaged quantities.

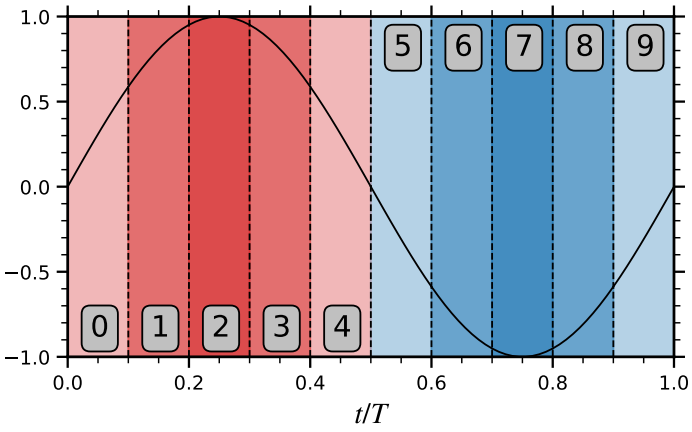

FIGURE 1: LABELING OF THE BINS WITH RESPECT TO A REFERENCE OSCILLATOR

Coherent components of double and triple correlations need to be evaluated to compute the turbulent stresses and all the terms involved in their budget. In a similar fashion as when Reynolds decomposition is used, practical formulations can be obtained as equation 5 shows for the double correlation.

$$\widetilde{a'b'} = \widetilde{ab} - \widetilde{a}\widetilde{b} - \widetilde{a}\overline{b} - \overline{a}\widetilde{b} + \overline{a}\overline{b} \tag{5}$$

The formulation for the triple correlation, needed only for the turbulent transport diffusion term, requires more operations and is therefore not given here for the sake of brevity.

3. RESULTS

3.1 Basic flow features

To highlight the various features of this flow, figure 2 shows instantaneous contours of density gradient magnitude at mid-span and streamwise velocity near the bump wall, at $y^+ \approx 10$. A fully turbulent boundary layer is observed upstream of the bump, with characteristic long streaks. Approaching the bump, the flow slightly decelerates on the concave part and then accelerates as it evolves on its convex part. The boundary layer partially re-laminarizes due to the favorable gradient there. As an effect, turbulence structures are expanding in the spanwise direction. An indicator of re-laminarization is the acceleration parameter [21], which exceeds here the threshold value 3.2×10^{-6}, with a peak value $\approx 2.4 \times 10^{-5}$. An oblique compression wave is generated when the flow separates. The remaining compression is performed by the normal shock-wave standing downstream. The

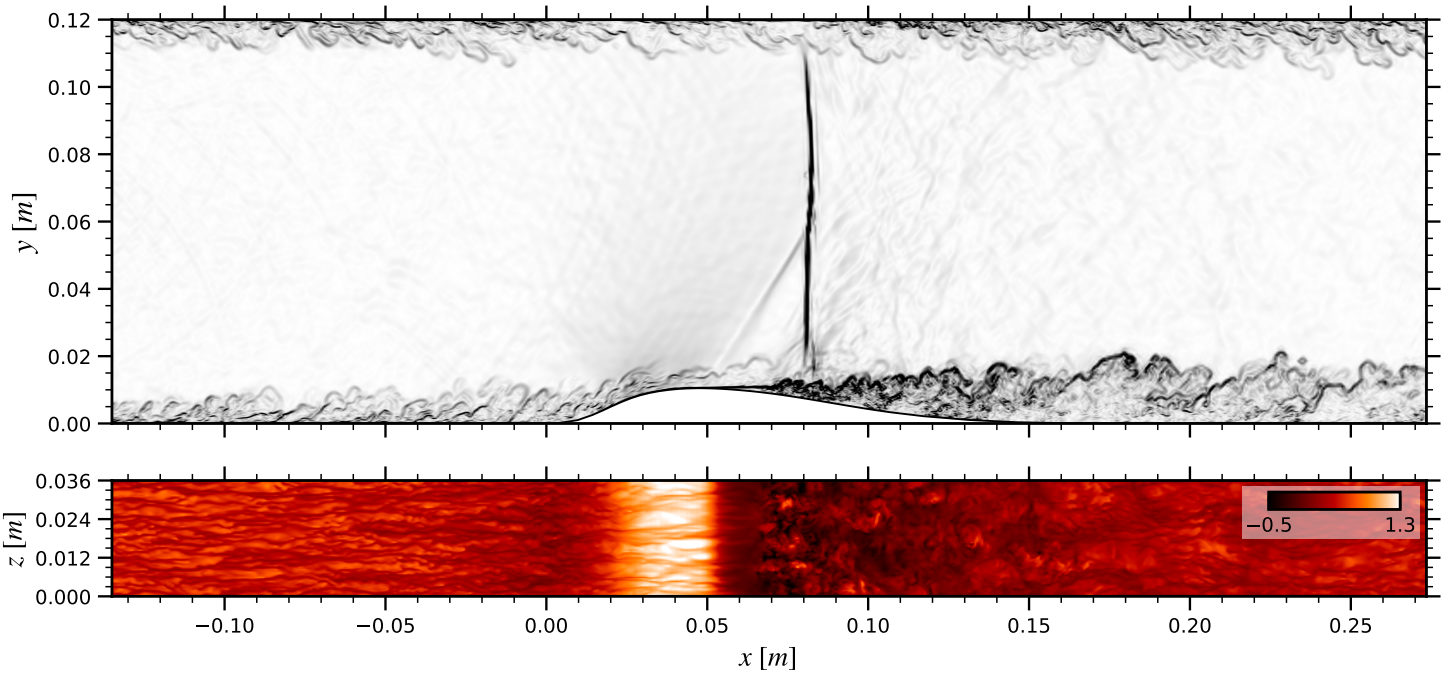

FIGURE 2: INSTANTANEOUS DENSITY GRADIENT MAGNITUDE AT MID-SPAN (*TOP*) AND u/U_∞ NEAR THE BUMP WALL, $y^+ \approx 10$ (*BOTTOM*)

separated shear layer is unstable, breaks down to turbulence and as a consequence, weak oblique compression waves are observed at the root of the normal shock. Finally, the boundary layer slowly recovers its initial, unperturbed state while reaching the end of the domain as streaks start to reappear. It is noted that the flow is drastically different compared to experimental results [2]. Indeed, re-laminarization is enhanced if viscosity is increased as it is the case in this simulation. As a consequence, the boundary layer is more prone to separation, which therefore occurs much earlier because of the adverse pressure gradient imposed by the geometry. In the experiment, re-laminarization is weaker and the boundary layer separates more downstream, due to the interaction with the shock.

The grid resolution is illustrated in figure 3. Upstream of the bump, the resolution is close to the target values $\Delta x^+ = 16$ and $\Delta z^+ = 12$. In the wall-normal direction, the very first solution point stands at a distance of $y^+ \approx 0.3$ from the wall. It is observed that the resolution remains around the target values or below, exception made of a short part of the bump over which it slightly worsens. At maximum, $\Delta x^+ \approx 30$, $\Delta z^+ \approx 20$ and $y^+ \approx 0.5$. Nevertheless, the resolution is still adequate for wall-resolved implicit large-eddy simulations.

Figure 4 shows the mean velocity profile in wall units, at the station $x = -0.135$m, upstream of the bump. The results are compared with DNS data for incompressible boundary layers [22] at the same Re_θ. The blue solid line indicates the Van Driest transformed velocity profile and is in perfect agreement with the incompressible normalization (black solid line) in the viscous sub-layer and the log layer. A slight difference is however observed in the defect layer. The same agreement is found with respect to the DNS data. Figure 5 depicts the normalized mean Reynolds stress profiles at the same station, again compared with DNS data from [22] and shows a very good fit. The overestimation of the peak $\overline{u'u'}$ is an effect of the under-resolution. These results show that the upstream boundary layer is properly developed and that compressibility effects are small in this case, even if the bulk Mach number is 0.7. The latter has been also highlighted in [23].

The mean friction coefficient and mean pressure coefficient on the bump wall are illustrated in figure 6. As the incoming flow is subsonic, the bump has an upstream influence which is observed on both coefficients. Nevertheless, the friction coefficient steadily decreases already before, which is another proof that the inflow is far enough from the bump for the turbulence to develop properly. The flow separates from around $x = 0.055$m to $x = 0.119$m. It is noted that the first location is slightly downstream the section throat ($x = 0.0476$m). The topology of the recirculation region is similar to previous studies [4, 6]. It consists first of a short stable part, which almost reattaches on rare occasions, and a second part, much larger and more unstable. The latter show a high variance in the friction coefficient that is linked to the vortex shedding taking place due to the breakdown of the separated shear layer. Regarding the pressure coefficient, the upstream influence of the bump is observed too. The minimum is located at the section throat. Downstream, pressure sharply rises as the flow undergoes compression from the oblique wave and the shock. The plateau observed in the pressure coefficient corresponds to the stable recirculation region. Finally, the boundary slowly recovers and static pressure reaches the imposed outlet value.

The mean turbulent stresses on the downstream part of the bump are illustrated in figure 7. Among the normal stresses, the streamwise component $\overline{u'u'}$ is dominant and is therefore the main contributor to the mean turbulent kinetic energy. It starts to be

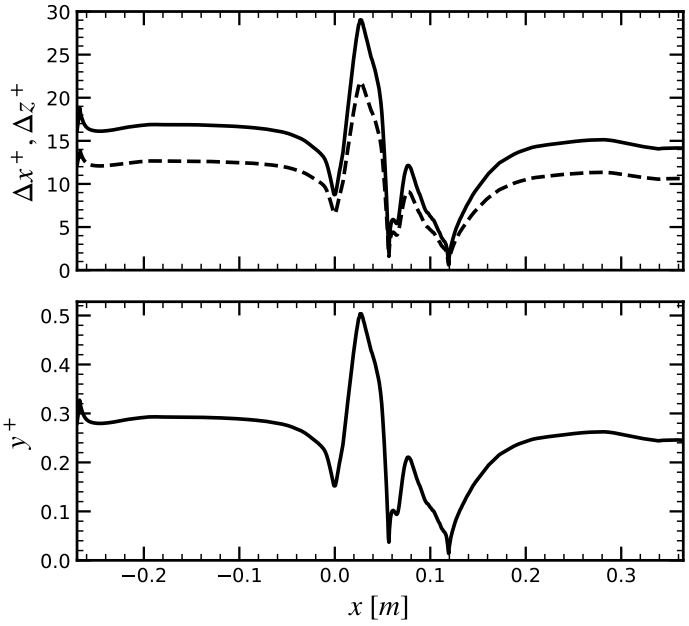

FIGURE 3: GRID RESOLUTION - Δx^+ (*TOP, SOLID*), Δz^+ (*TOP, DASHED*) AND y^+ (*BOTTOM*)

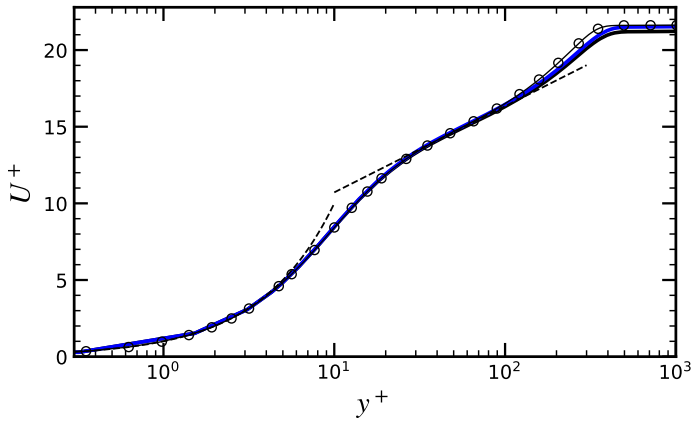

FIGURE 4: MEAN VELOCITY PROFILE AT $x = -0.135m$ IN VISCOUS UNITS - INCOMPRESSIBLE NORMALIZATION ((SOLID BLACK)) AND VAN DRIEST NORMALIZATION (*SOLID BLUE*) COMPARED WITH DNS DATA [22] (*SYMBOLS*)

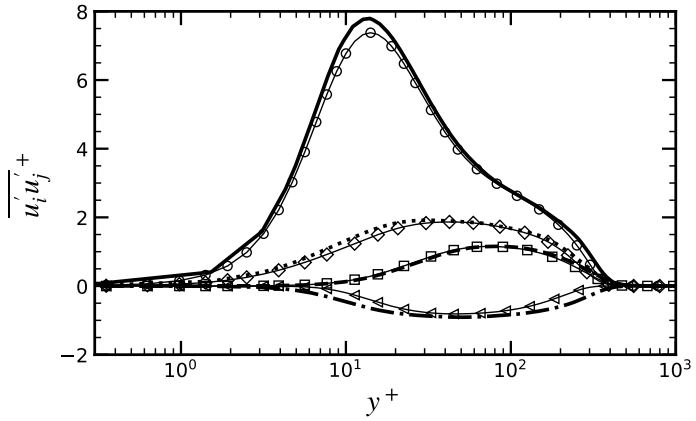

FIGURE 5: PROFILES OF NORMALIZED REYNOLDS STRESSES AT $x = -0.135m$ - $\overline{u'u'}$ (*SOLID*), $\overline{v'v'}$ (*DASHED*), $\overline{w'w'}$ (*DOTTED*) AND $\overline{u'v'}$ (*DASHDOT*) COMPARED WITH DNS DATA [22] (*SYMBOLS*)

produced as soon as the flow separates and maximum values are found along the mixing layer. The two other normal components are of similar magnitude (even though $\overline{w'w'} > \overline{v'v'}$) and are produced more downstream, in the recirculation region. The mean shear stress is not negligible and shares the the same features as $\overline{v'v'}$ and $\overline{w'w'}$.

To obtain insights on the influence of the oscillating back-pressure, the pre-multiplied weighted power spectral density of wall static pressure has been computed based on signals at various streamwise positions and the result is shown in figure 8. Different locations are highlighted by vertical white lines to ease the analysis. These locations are, from left to right, the beginning of the bump, the bump throat, the end of the stable separated region, the reattachment point and the end of the bump. The upstream boundary layer is characterized by the ridge centered around 50 kHz. A clear influence of the forcing frequency is observed once the boundary layer separates and persists at almost all streamwise locations. It is interesting to note that the stable recirculation bubble acts as a low-pass filter, the forcing frequency being the only contributor. Downstream of it, lower frequencies can be detected and form a second ridge. It is corresponding to the downstream boundary layer, which is thicker than the upstream one. Therefore, the associated energetic turbulent structures are bigger and this leads to larger timescales or lower frequencies.

Figure 9 illustrates the static wall pressure amplitude at the forcing frequency $A_{\widetilde{p}_w}$, normalized by the amplitude of the imposed outlet static pressure $A_{\widetilde{p}_o}$. Pressure fluctuations follow a complex pattern of successive amplification and attenuation that can be linked to other flow features. First and second amplification peaks correspond respectively to the mean separation point (≈ 0.055m) and the minimum of friction coefficient (≈ 0.075m). On the attenuation side, first and third peaks are associated to the end of the stable bubble ($x \approx 0.065$m) and the third is located near the end of the bump ($x \approx 0.18$m).

The behavior of other flow features with respect to the forcing has been investigated in more details in a previous work [24]. It has been shown that the shock moves primarily at the forcing frequency, with its upper part following up to three harmonics. The separation and the reattachment points mainly respond at the forcing frequency too.

3.2 Coherent flow

3.2.1 Reference oscillator. As explained in the methodology section, phase-average is employed to extract the coherent component of the flow variables and this requires the definition of a reference oscillator. It has been shown previously [24] that the dominant contribution to the evolution of the separation point position is due to the forcing. A reference oscillator is then obtained by reconstructing the signal with the sole contribution of the forcing frequency, its magnitude and phase being computed using FFT of the original signal. The resulting reconstructed signal is illustrated in figure 10 on top of the original signal. The

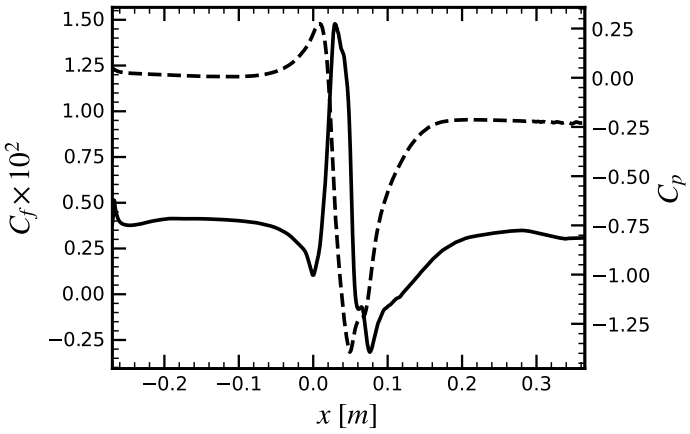

FIGURE 6: MEAN FRICTION COEFFICIENT (*SOLID*) AND MEAN PRESSURE COEFFICIENT (*DASHED*)

low-frequency trend at the forcing frequency is clearly visible. With respect to the labeling introduced in figure 1, bins 2 and 7 correspond therefore to the most downstream and most upstream locations of the separation point respectively.

Other flow features could have been considered to serve as reference oscillator since many of them (shock position, wall pressure, etc.) respond primarily to the forcing frequency. However, the perturbation imposed here is an upstream propagating plane wave. The different regions of the flow are therefore not affected in the same way at the same time. The key benefit in using the separation point is its proximity to the regions of interest for this study, namely the mixing layer and the recirculation. It will ensure a better description of the coherent flow in those regions, compared to regions located more downstream. For instance, the phase lag between the separation point and the lowest point of the shock is around 60°. As a consequence, building the reference oscillator based on the shock position will result in an improper classification of the samples because of the translation of the reconstructed signal.

3.2.2 Streamwise velocity. Figure 11 shows the time history of the coherent streamwise velocity $\widetilde{u}$. In the freestream, an upstream propagating wave is clearly discerned, which is the result of the forcing. Moreover, this wave is of opposite sign compared to the pressure wave. In the freestream, the momentum equation in the streamwise direction for the coherent motion can be indeed simplified such that

$$\overline{u}\frac{\partial \widetilde{u}}{\partial x} = -\frac{1}{\rho}\frac{\partial \widetilde{p}}{\partial x} \tag{6}$$

and therefore pressure forces balance convection. On the rear part of the bump, a massive coherent structure is observed. It starts from the separation point and develops as a consequence of the mixing layer. It is further convected downstream as it changes of sign. It is noted that when the separation point location is the most downstream (bin 2), this structure exhibits highly positive values and changes sign as the separation point moves upstream. This is in concordance with the motion of the weak oblique compression wave emanating from the separation point.

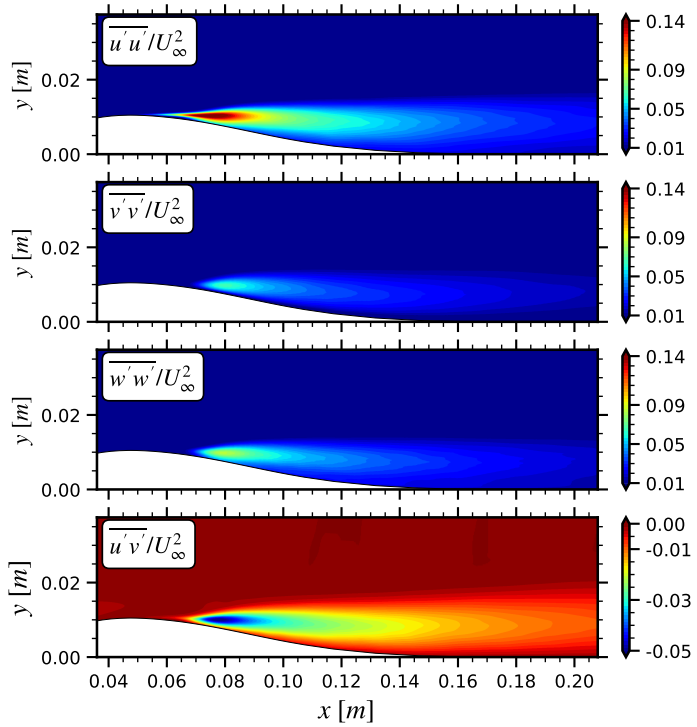

FIGURE 7: MEAN TURBULENT STRESSES ON THE DOWNSTREAM PART OF THE BUMP

In order to check statistical convergence, it is interesting to compare the phase-averaged or coherent flow variables to their smooth reconstruction. As an example, figure 12 shows the coherent streamwise velocity at a point in the mixing layer and the first harmonic of its Fourier transform. The low scatter between the data points and its reconstruction shows that a good convergence has been reached. At this point, the first mode corresponds to more than 97% of the total harmonic content, meaning that u is evolving mainly at the forcing frequency. Besides the freestream, the first mode has been found to be dominant in the coherent structure mentioned above and at the oblique compression wave, with more than 90% of the total harmonic content.

3.2.3 Turbulent stresses. The time history of $\widetilde{u'u'}$ is depicted in figure 13. Various coherent structures are observed starting from the separation point and two layers are discerned. The top layer is constituted of a single and stable structure which coincides well with the mixing layer. When the separation point is positioned more downstream than its mean location (bins 0 to 4), $u'u'$ is decreasing since the coherent component is negative. The opposite happens for bins 5 to 9, in which the separation point lies more upstream. A sudden change in sign is noticed when switching the regime. These observations give confidence in the choice of the reference oscillator.

The composition of the bottom layer is more variable. For the two extreme bins, three structures are clearly identified. The first structure starting from the separation point is of the opposite sign compared to the top layer structure. Then, the sign successively alternates. For other bins, the picture is more complicated. The bottom layer structures are collapsing or growing and therefore are less stable compared to the single top layer structure.

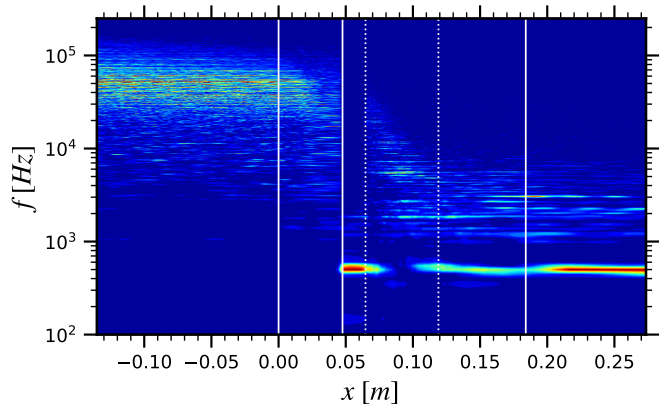

FIGURE 8: PRE-MULTIPLIED WPSD MAP OF WALL STATIC PRESSURE

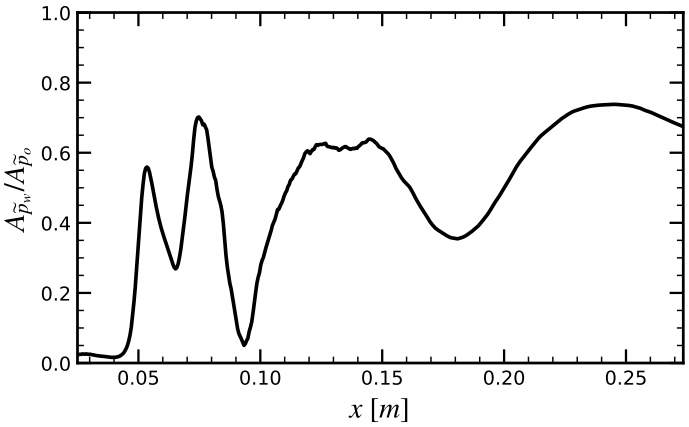

FIGURE 9: NORMALIZED WALL STATIC PRESSURE AMPLITUDE AT 500 HZ

Looking at the coherent $\widetilde{u'u'}$ in the mixing layer in figure 14, the first harmonic captures very well the trend. A bigger scatter is observed compared to what has been shown for $\widetilde{u}$ in figure 12. This simply comes from the fact that higher-order statistics take longer to converge. However, 93% of the total harmonic content still comes from the forcing frequency.

In terms of amplitude, the coherent component of $u'u'$ is one order of magnitude smaller than its mean component (depicted in figure 7) when considering maximum values. However, comparing local values shows that in some regions the coherent component is larger than half the mean and cannot be neglected. To illustrate this, figure 15 shows the profiles of the three first harmonics of $\widetilde{u'u'}$ compared to the local mean value $\overline{u'u'}$, along a gridline starting from $x \approx 0.07$m. Close to the wall, the first harmonic account already for around 15% of the mean value. In the mixing layer ($h \approx 3 \times 10^{-3}$m), the first harmonic reaches 60%. Even the second harmonic is noticeable, contributing to 10% close to the wall and around 25% in the mixing layer.

Similar results have been found for the other turbulent stresses, namely $u'v'$, $v'v'$ and $w'w'$ but are not shown for the sake of brevity. Their amplitude is nevertheless lower than for $u'u'$, which is in line with the description of the mean stresses. It also means that $\widetilde{u'u'}$ is the main contributor to the oscillatory (or coherent) turbulent kinetic energy.

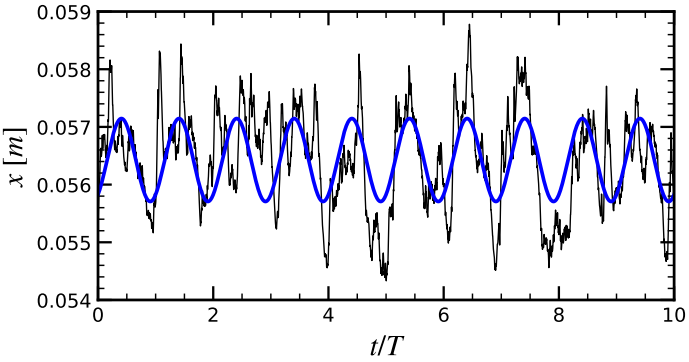

FIGURE 10: SEPARATION POINT LOCATION (*BLACK*) AND REFERENCE OSCILLATOR (*BLUE*)

3.2.4 Turbulent stress budgets. To obtain deeper insights on the behavior of the oscillatory turbulence, all the budgets terms have been computed. The analysis will be performed here for $\widetilde{u'u'}$ since it has been shown that it is the largest contributor to the oscillatory kinetic energy $\widetilde{k}$, as in steady flow. Among all the terms, only a few are noticeable.

The production $\widetilde{P}_{11}$ comes mainly from two terms (out of eight), $-2\widetilde{u'v'}\partial\widetilde{u}/\partial y$ and $-2\widetilde{u'v'}\partial\overline{u}/\partial y$. It is illustrated in figure 16 by comparing the sum of all production terms to these two dominant ones. These are representing respectively the action of the coherent flow upon the mean component of the shear stress and the action of the mean flow upon the coherent component of the mean shear stress. Even though these results have been obtained in a separated flow, these are in agreement with experimental observations on attached turbulent boundary layers subjected to oscillatory shear [20]. It is also interesting to notice the different regions of action of each term, the first one acting on the bottom layer and the second one on the top layer.

Besides production, other noticeable contributions are convection, pressure strain and turbulent diffusion. Interestingly, pressure strain is acting on the top layer, partially balancing the second production term, as also depicted in figure 16. In addition, the shock region is largely influenced by pressure strain. This result should however be taken cautiously since the budget equations are derived for an incompressible flow and this assumption is not valid around the shock.

4. CONCLUSION

A wall-resolved implicit large-eddy simulation of a transonic bump in forced conditions has been performed. Particular attention has been given to reproduce actual turbomachinery flow conditions: a shock-wave interacts with the separated boundary layer in the blade passage and a fluctuating backpressure mimics the effect of the rotor/stator interaction.

The focus of the analysis being on the coherent flow, phase-averaging has been carried out. The reference oscillator has been built on the location of the separation point and has been proven to be adequate in extracting this component. Statistical convergence of the bins has been checked by comparing coherent quantities to their smooth Fourier reconstruction. It also allowed

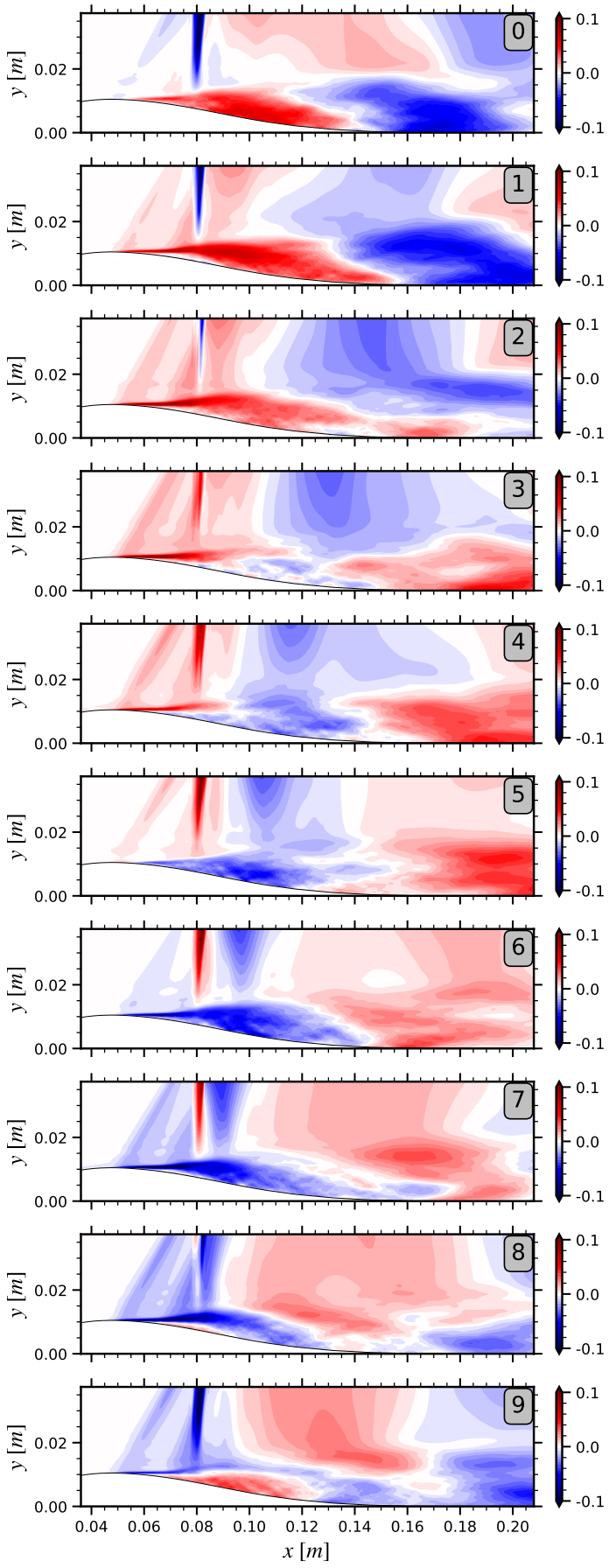

FIGURE 11: TIME HISTORY OF $\widetilde{u}/U_\infty$

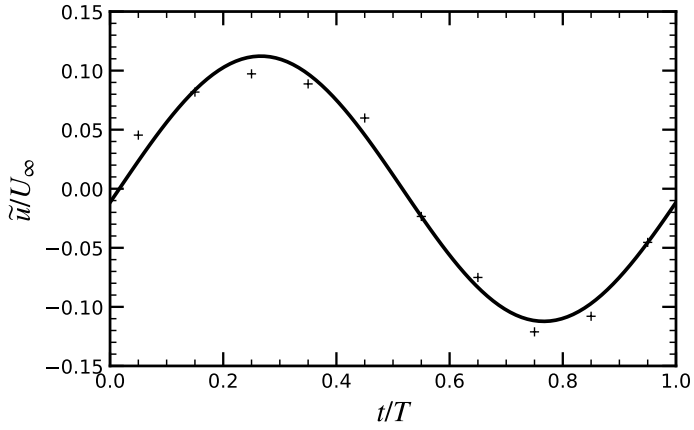

FIGURE 12: COHERENT STREAMWISE VELOCITY IN THE MIXING LAYER - PHASE-AVERAGED VALUES (*SYMBOLS*) AND FIRST HARMONIC RECONSTRUCTION (*SOLID*)

to highlight coherent structures in the streamwise velocity, the turbulent stresses and their budget terms.

More specifically, the dominant oscillatory turbulent stress, namely $\widetilde{u'u'}$, exhibits a two-layers pattern. The top layer follows clearly the mixing layer, whereas an inner layer develops below with several successive coherent structures. Its amplitude is significant when compared to local mean amplitude. In the mixing layer, it can be as high as 60% of the mean.

Production terms and pressure strain are among the main contributors to the transport equations of the coherent turbulent stresses. For $\widetilde{u'u'}$, it has been shown that two production terms are involved. The first one, representing the action of the coherent flow upon the mean shear stress, is significant in the inner layer whereas the second, associated to the action of the mean flow against the coherent shear stress, is mainly present in the mixing layer. Whereas these results are related to a massively separated flow, it is noted that some links have been made with experimental observations on oscillatory attached boundary layers.

It is believed that the current results give valuable insights for turbulence modelers. In particular, the data produced with the simulation presented in this work could be used to develop a model for the harmonic turbulence. This could allow to get rid of the frozen turbulence assumption often used in frequency-domain methods such as the Non-Linear Harmonic method [25]. Investigations are pursued in that direction.

ACKNOWLEDGMENTS

This project has received funding from the European Union's Horizon 2020 research and innovation programme under the grant agreement MSCA-ITN-ETN TEAMAero No 860909. The authors would also like to thank Prof. Charles Hirsch for bringing this initiative within Cadence Design Systems and for his support during this work.

REFERENCES

[1] Tucker, PG. "Computation of Unsteady Turbomachinery Flows: Part 1—Progress and Challenges." *Progress in Aerospace Sciences* Vol. 47 No. 7 (2011): pp. 522–545. DOI 10.1016/j.paerosci.2011.06.004.

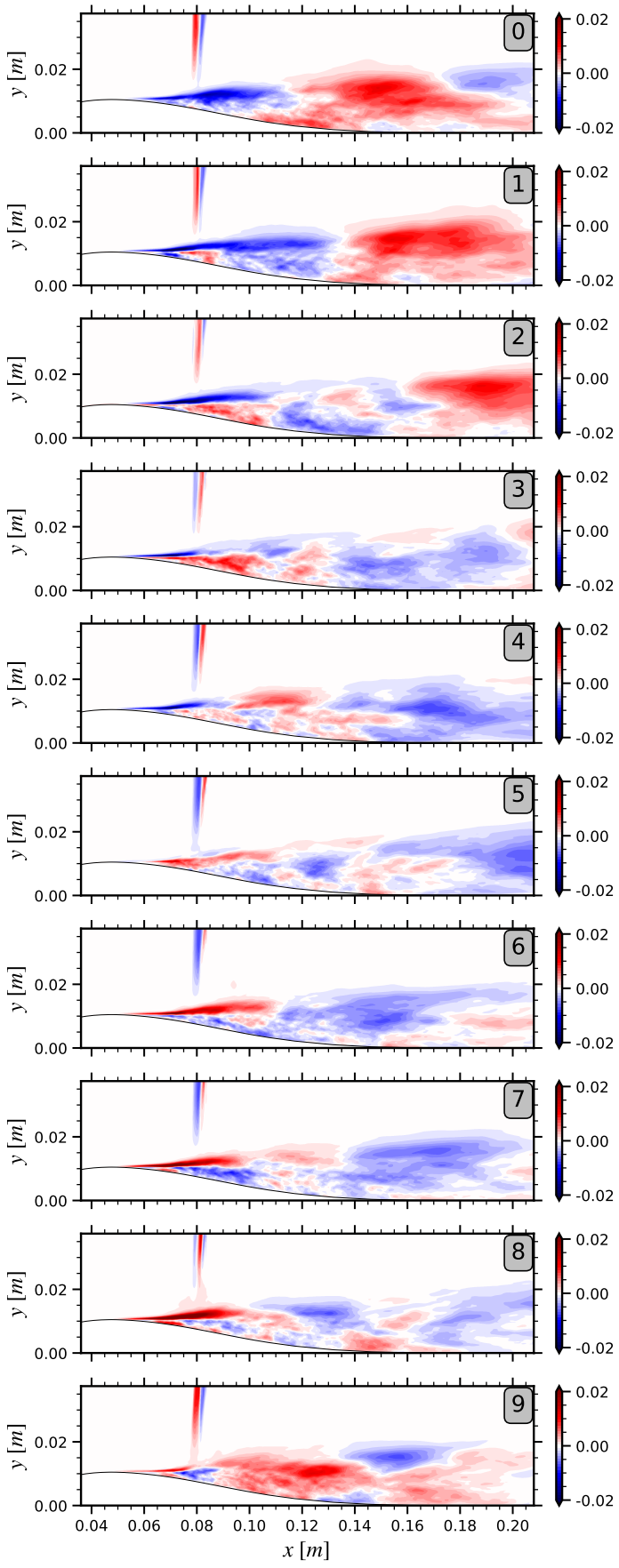

FIGURE 13: TIME HISTORY OF $\widetilde{u'u'}/U_\infty^2$

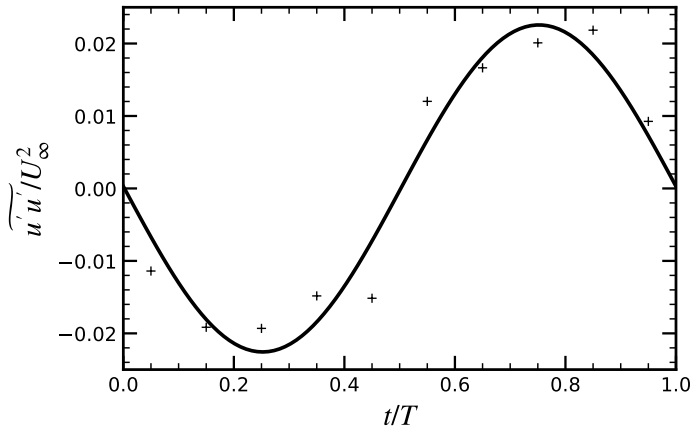

FIGURE 14: COHERENT $u'u'$ IN THE MIXING LAYER - PHASE-AVERAGED VALUES (*SYMBOLS*) AND FIRST HARMONIC RECONSTRUCTION (*SOLID*)

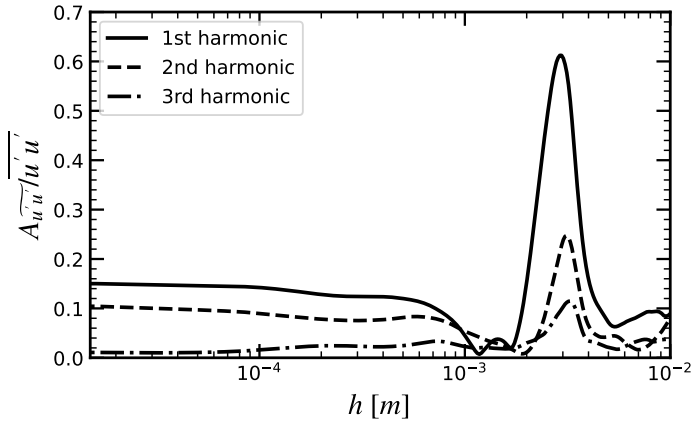

FIGURE 15: PROFILES OF AMPLITUDE OF THE THREE FIRST HARMONICS OF $\widetilde{u'u'}$ WITH RESPECT TO ITS MEAN VALUE

[2] Bron, O. "Numerical and Experimental Study of the Shock-Boundary Layer Interaction in Transonic Unsteady Flow." Ph.D. Thesis, Royal Institute of Technology, Sweden. 2003.

[3] He, L and Ning, W. "Efficient Approach for Analysis of Unsteady Viscous Flows in Turbomachines." *AIAA Journal* Vol. 36 No. 11 (1998): pp. 2005–2012. DOI 10.2514/2.328.

[4] Wollblad, Christian, Davidson, Lars and Eriksson, Lars-Erik. "Large Eddy Simulation of Transonic Flow with Shock Wave/Turbulent Boundary Layer Interaction." *AIAA Journal* Vol. 44 No. 10 (2006): pp. 2340–2353. DOI 10.2514/1.20358.

[5] Wollblad, Christian, Davidson, Lars and Eriksson, L-E. "Investigation of Large Scale Shock Movement in Transonic Flow." *International Journal of Heat and Fluid Flow* Vol. 31 No. 4 (2010): pp. 528–535. DOI 10.1016/j.ijheatfluidflow.2010.02.009.

[6] Brouwer, Jens. "A Study of Transonic Shock-Wave/Boundary-Layer Interactions Using Conservative, Skew-Symmetric Finite-Differences." Ph.D. Thesis, Technische Universitaet Berlin, Germany. 2016.

[7] Bodin, Olle and Fuchs, Laszlo. "Shock Unsteadiness and Shock Induced Separation at Transonic Flow over a Bump."

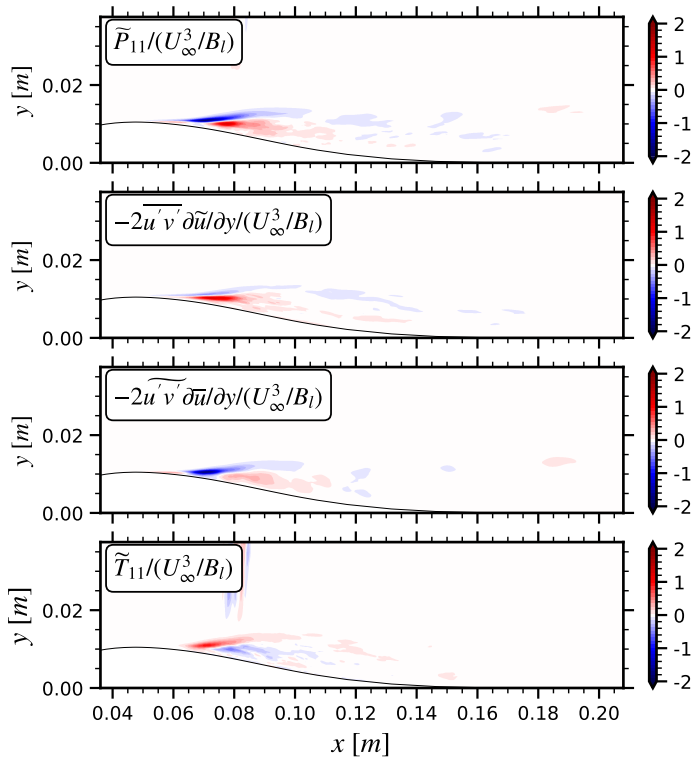

FIGURE 16: TOTAL PRODUCTION, DOMINANT PRODUCTION TERMS AND PRESSURE STRAIN FOR BIN 2

38th Fluid Dynamics Conference and Exhibit: p. 4174. 2008. DOI 10.2514/6.2008-4174.

[8] Huynh, H. T. "A Flux Reconstruction Approach to High-Order Schemes Including Discontinuous Galerkin Methods." *18th AIAA Computational Fluid Dynamics Conference*: p. 4079. 2007. DOI 10.2514/6.2007-4079.

[9] Carpenter, M. H. and Kennedy, C. A. "Fourth-Order 2N-storage Runge-Kutta Schemes." (1994).

[10] Persson, Per-Olof and Peraire, Jaime. "Sub-Cell Shock Capturing for Discontinuous Galerkin Methods." *44th AIAA Aerospace Sciences Meeting and Exhibit*: p. 112. 2006. DOI 10.2514/6.2007-4079.

[11] Ducros, F, Ferrand, V, Nicoud, Franck, Weber, C, Darracq, D, Gacherieu, C and Poinsot, Thierry. "Large-Eddy Simulation of the Shock/Turbulence Interaction." *Journal of Computational Physics* Vol. 152 No. 2 (1999): pp. 517–549. DOI 10.1006/jcph.1999.6238.

[12] Wang, C., Zhang, X., Shu, C. W. and Ning, J. "Robust High Order Discontinuous Galerkin Schemes for Two-Dimensional Gaseous Detonations." *Journal of Computational Physics* Vol. 231 No. 2 (2012): pp. 653–665. DOI 10.1016/j.jcp.2011.10.002.

[13] Klein, M., Sadiki, A. and Janicka, J. "A Digital Filter Based Generation of Inflow Data for Spatially Developing Direct Numerical or Large Eddy Simulations." *Journal of Computational Physics* Vol. 186 No. 2 (2003): pp. 652–665. DOI 10.1016/S0021-9991(03)00090-1.

[14] Xie, Z. T. and Castro, I. P. "Efficient Generation of Inflow Conditions for Large Eddy Simulation of Street-Scale Flows." *Flow, Turbulence and Combustion* Vol. 81 No. 3 (2008): pp. 449–470. DOI 10.1007/s10494-008-9151-5.

[15] Adler, Michael C, Gonzalez, David R, Stack, Cory M and Gaitonde, Datta V. "Synthetic Generation of Equilibrium Boundary Layer Turbulence from Modeled Statistics." *Computers & Fluids* Vol. 165 (2018): pp. 127–143. DOI 10.1016/j.compfluid.2018.01.003.

[16] Lund, T. S., Wu, X. and Squires, K. D. "Generation of Turbulent Inflow Data for Spatially-Developing Boundary Layer Simulations." *Journal of Computational Physics* Vol. 140 No. 2 (1998): pp. 233–258. DOI 10.1006/jcph.1998.5882.

[17] Goffart, N., Tartinville, B., Puri, K., Hirsch, C. and Pirozzoli, S. "High-Order, High-Fidelity Simulation of Unsteady Shock-Wave/Boundary Layer Interaction Using Flux Reconstruction." *8th European Congress on Computational Methods in Applied Sciences and Engineering*. 2022. DOI 10.23967/eccomas.2022.138.

[18] Sigfrids, Timmy. "Hot Wire and PIV Studies of Transonic Turbulent Wall-Bounded Flows." Licentiate thesis, Royal Institute of Technology, Sweden. 2003.

[19] Reynolds, WC and Hussain, AKMF. "The Mechanics of an Organized Wave in Turbulent Shear Flow. Part 3. Theoretical Models and Comparisons with Experiments." *Journal of Fluid Mechanics* Vol. 54 No. 2 (1972): pp. 263–288. DOI 10.1017/S0022112072000679.

[20] Brereton, GJ and Reynolds, WC. "Dynamic Response of Boundary-Layer Turbulence to Oscillatory Shear." *Physics of Fluids A: Fluid Dynamics* Vol. 3 No. 1 (1991): pp. 178–187. DOI 10.1063/1.857877.

[21] Jones, W Peter and Launder, Brian Edward. "The Prediction of Laminarization with a Two-Equation Model of Turbulence." *International Journal of Heat and Mass Transfer* Vol. 15 No. 2 (1972): pp. 301–314. DOI 10.1016/0017-9310(72)90076-2.

[22] Schlatter, Philipp and Örlü, Ramis. "Assessment of Direct Numerical Simulation Data of Turbulent Boundary Layers." *Journal of Fluid Mechanics* Vol. 659 (2010): pp. 116–126. DOI 10.1017/S0022112010003113.

[23] Wenzel, Christoph, Selent, Björn, Kloker, Markus and Rist, Ulrich. "DNS of Compressible Turbulent Boundary Layers at Varying Subsonic Mach Numbers." *47th AIAA Fluid Dynamics Conference*: p. 3116. 2017. DOI 10.2514/6.2017-3116.

[24] Goffart, N., Tartinville, B., Hirsch, C. and Pirozzoli, S. "Investigation of Forced Shock-Induced Separation in a Transonic Channel." *Proceedings of 15th European Conference on Turbomachinery Fluid dynamics & Thermodynamics*. 2023.

[25] Vilmin, S, Lorrain, E, Hirsch, Ch and Swoboda, M. "Unsteady Flow Modeling Across the Rotor/Stator Interface Using the Nonlinear Harmonic Method." *Turbo Expo: power for land, sea, and air*, Vol. 4241: pp. 1227–1237. 2006. DOI 10.1115/GT2006-90210.